JASA ARTICLE

Guidelines for higher efficiency supported thermo-acoustic emitters based on periodically Joule heated metallic films

Boris Leizeronok, Slava Losin, Alex Kleiman, Shimon Julius, Iliya Romm, and Beni Cukurel[a)]
Turbomachinery and Heat Transfer Laboratory, Technion-IIT, Haifa, 3200003, Israel

ABSTRACT:
The paper focuses on the evaluation of the impact associated with various geometrical and material properties on the overall acoustic performance of generic multi-layer thermo-acoustic sources. First, a generalized numerical framework is developed using a state-of-the-art thermo-acoustic emission model for multi-layered devices and is used to forecast the effects associated with different parameters (thickness, density, thermal conductivity, and specific heat capacity), based on a set of 65 536 simulated architectures. Then, the acoustic facility is designed, assembled, and instrumented, and the findings of the simulation campaign are validated against experimental measurements for 32 different samples, manufactured via various vacuum deposition techniques. The results of the experimental campaign corroborate the simulation's prediction and indicate that the variables that have the strongest impact on the thermo-acoustic performance are the thicknesses of the substrate and thermophone layers, as well as the backing's thermal conductivity. Finally, the experimental results are directly comparable with the simulation predictions and the deviation between the two values is within the limits of the experimental accuracy, with an average deviation of 12% (maximal divergence of 28%) and best absolute performance of 0.018 [Pa/W] when measured from a distance of 75 [mm]. Overall, the findings provide an insight into the effect of analyzed properties and offer a set of tangible guidelines that can be applied in the future toward the design optimization process that can potentially result in higher-efficiency thermophone-on-substrate thermo-acoustic emitters. https://doi.org/10.1121/10.0017598

(Received 12 October 2022; revised 15 February 2023; accepted 23 February 2023; published online 14 March 2023)

[Editor: Robert D. White] Pages: 1682–1693

NOMENCLATURE

Variables

$B\,[Pa]$	Bulk modulus
$C_P\,[J\,kg\,K^{-1}]$	Specific heat capacity at constant pressure
$C_V\,[J\,kg\,K^{-1}]$	Specific heat capacity at constant volume
$\mathcal{F}$, $\mathcal{G}\,[-]$	General functions
$L\,[m]$	Layer thickness, thermophone dimensions
$R_a\,[m]$	Mean profile deviation
$R_q\,[m]$	Root mean square surface roughness
$S_0\,[W\,m^{-3}]$	Supplied thermal power density
$SP\,[-]$	Speed up ratio
$T\,[K]$	Temperature
$T_0\,[K]$	Ambient temperature
$W\,[W]$	Radiated sound power
$b\,[N]$	External force
$c\,[m\,s^{-1}]$	Speed of sound
$f_p\,[-]$	Parallelizable code portion
$g\,[-]$	Number of cores
$i\,[-]$	Imaginary root of $\sqrt{-1}$
$k\,[m^{-1}]$	Wave number
$p\,[Pa]$	Pressure
$q\,[W\,m^{-2}]$	Heat flux
$r\,[m]$	Distance
$u\,[m]$	Particle displacement
$v\,[m\,s^{-1}]$	Particle velocity
$x, y, z\,[m]$	Spatial coordinates
$\alpha\,[-]$	Ratio between source dimensions
$\alpha_T\,[K^{-1}]$	Volumetric expansion coefficient
$\gamma\,[-]$	Heat capacity ratio
$\eta_{th}\,[-]$	Mean thermal efficiency
$\kappa\,[W\,m^{-1}\,K^{-1}]$	Thermal conductivity
$\lambda\,[Pa\,s]$	First viscosity coefficient
$\lambda_0\,[Pa]$	First Lamé elastic coefficient
$\mu\,[Pa\,s]$	Second viscosity coefficient
$\mu_0\,[Pa]$	Second Lamé elastic coefficient
$\xi\,[-]$	General parameter
$\rho\,[kg\,m^{-3}]$	Density

Acronyms

CPU	Central Processing Unit
RMS	Root Mean Square
SPL	Sound Pressure Level

Chemical Elements

Au	Gold
Pt	Platinum
Pd	Palladium

[a)]Electronic mail: beni@cukurel.org

https://doi.org/10.1121/10.0017598

Ru	Ruthenium
Si_3N_4	Silicon Nitride
SiO_2	Silicon Dioxide

Subscripts and Superscripts

FF	Far field
g	Gas
j	Layer number
sub	Substrate
th	Thermophone

I. INTRODUCTION

Pressure field stimulation and sound production via Joule heating effect have been studied since the late 19th century, after being first noticed by Braun in a bolometer, where the passage of an alternating current through a thin wire was observed to result in sound generation (Braun, 1898). The term "thermophone" was introduced by De Lange two decades later, to define an acoustic transmitter capable of producing sound through thermal oscillations (De Lange, 1915). These devices behave as electrical resistors, where an alternating electrical current is converted to produce surface heat flux fluctuations and, consequently, pressure waves in the surrounding fluid, absent of mechanical motion (Hu *et al.*, 2012a). Therefore, such transducers can offer a number of potential advantages over conventional vibro-acoustic devices owing to their design simplicity, lightweight structure, acoustic purity, and broad frequency range (Arnold and Crandall, 1917; Xiao *et al.*, 2008).

After its initial discovery, the thermo-acoustic effect remained largely unexplored for several decades. However, due to recent introduction of novel materials and fabrication methods, at the turn of the 21st-century, thermophones regained the scientific community's interest with a seminal paper that described the construction of aluminum film ultrasound generators held midair by porous silicon (Shinoda *et al.*, 1999). In contrast to the early 20th century's thermophones, which were constructed from simple thin metal wires, this configuration introduced a thermally and electrically insulated backing. The impact of this additional layer on the thermo-acoustic energy conversion process was examined experimentally using several similarly structured thermo-acoustic emitters (thin heated films over substrate material) and it was shown that the applied substrate also plays a significant role in sound production (Boullosa and Santillan, 2004). Moreover, significant efforts have been invested to characterize the behavior of thermophones in different gaseous and liquid media (Aliev *et al.*, 2010; Daschewski, 2016; Wente, 1922; Xiao *et al.*, 2011). Furthermore, advanced designs with suspended arrays of aluminum wires, carbon nanotubes, and graphene were developed to explore the efficiency and performance envelopes of heat flux sound sources (Aliev *et al.*, 2013; Barnard *et al.*, 2013; Bouman *et al.*, 2016; Niskanen *et al.*, 2009; Xiao *et al.*, 2008). However, there is no clear consensus in the literature as to the correct approach to modelling thermophone sound production.

The first attempt to model the thermo-acoustic emission appears in a paper by Arnold and Crandall from the AT&T Research Laboratory (Arnold and Crandall, 1917). This work predicts the periodic temperature variation in a thin platinum strip connected to a source of superimposed direct and alternating current under the assumption that part of the produced heat is transferred to surrounding medium and the remainder is stored in the strip and demonstrates more efficient acoustic generation with decreasing heat capacity per unit volume. The temperature fluctuations are then used to estimate thermal expansions and contractions in a small portion of the gaseous medium adjacent to the conductor, whose thickness depends on the source frequency and the medium's thermal diffusivity. The thermal fluctuations in turn give rise to sound waves. Noticing some discrepancies between this early model and the available experimental data, Wente presents a more detailed analysis that draws a parallel between the thermophone action and a diaphragm source with small mass and stiffness, actuated by a constant alternating force (Wente, 1922). Both systems produce similar pressure fluctuations in the neighboring air layer and enable calculation of the pressure developed in a small control volume around the heating source.

This "piston"-based model is still common in contemporary thermo-acoustic studies to predict generated sound based on heat flow balance equations, which account for convection, conduction, and radiation losses, as well as for stored heat. However, although piston-based formulation is sufficiently accurate in numerous cases, it has limitations in terms of system geometry and input parameters. Alternatively, classical conservation laws can also be implemented to describe thermo-acoustic generation. Originally derived to study the photo-acoustic effect (McDonald and Wetsel, 1978), the coupled equations for thermal and acoustic waves were recently solved in the context of thermo-acoustics to predict the acoustic performance of a flat thermophone deposited on a substrate and surrounded by perfect gas (Hu *et al.*, 2010). A similar methodology can be derived to study thermo-acoustic emission from spherical thermophones that act as acoustic monopoles (Hu *et al.*, 2012b), cylindrical geometries (Yin and Hu, 2017), and after further generalization, arbitrary sources (Hu *et al.*, 2014). Finally, in a bid to benefit from both formulations, there are several works in the literature, which suggest merging the continuum mechanics equations with the thermal balance approach of the piston-based framework (Lim *et al.*, 2013; Liu *et al.*, 2018; Tong *et al.*, 2015).

However, most of these prior numerical modeling efforts stem from the need to represent their empirical experimental data in a reduced form. Therefore, they typically omit various physics in the simulation environment, which are shown to play a potentially important role under different investigations (Aliev *et al.*, 2018; Brown *et al.*, 2016). Instead of relying on these simplification-driven paradigms and toward creating a generalized bottom-up

approach, the paper authored by Guiraud *et al.* (2019a) proposes a novel modular framework that can describe an arbitrary multi-layered thermophone device, where each layer is either a solid or a fluid. In this approach, the solid layers represent the active element of the thermo-acoustic emitter, its backing, adhesion films, and any other physical component of the thermophone. The fluid layers can be used to depict the propagation medium, gaps, and any other gaseous or liquid part of the system. In the following, the model provides a set of differential equations with full thermo-visco-elastic coupling for arbitrary planar thermophone geometries, including thermal and viscous dissipation. In this approach, the basic equations of continuum mechanics are rewritten to have a similar one-dimensional form for both fluids and solids. The general solution is obtained in matrix form and includes relevant physical properties in each layer, while considering plane wave propagation in all layers of the structure.

In order to acquire the performance driving properties and their relative importance trade-offs in typical multi-layered thermophones, a large number of evaluation data is required. In this paper, the methodology described in Guiraud *et al.* (2019a) is adapted for highly parallel computing and evaluated over a broad parameter range. In the following, a thorough experimental campaign is conducted to validate the trends and highlight the relative importance of each design variable. According to the authors' best knowledge, this is the first effort in the scientific literature that not only studies the impact of various properties associated with the layers of a particular thermophone structure but instead analyzes the comparative significance of individual geometric and material parameters, as well as their compound effect and bounds of relevance. Thus, the obtained set of experimentally validated guidelines defines the marginal benefit of improving each variable as a part of a complex cost function in thermophone design optimization, ultimately leading to higher-efficiency electro-thermo-acoustic conversion.

II. THERMOPHONE SIMULATION FRAMEWORK

A. Thermophone performance model

The implemented thermo-acoustic performance model is based on a description of a generalized multi-layer thermophone structure with an arbitrary number of solid and fluid layers (Guiraud *et al.*, 2019a). In fluids, the main balance equations rely on the conservation of mass, momentum, and energy (Landau and Lifschitz, 1986a),

$$\begin{aligned}
&\frac{1}{B}\frac{\partial p}{\partial t} = \alpha_T \frac{\partial T}{\partial t} - \vec{\nabla}\cdot\vec{v},\\
&\rho\frac{\partial \vec{v}}{\partial t} = -\vec{\nabla}p + \mu\nabla^2\vec{v} + (\lambda+\mu)\vec{\nabla}(\vec{\nabla}\cdot\vec{v}),\\
&\rho C_P\frac{\partial T}{\partial t} = \kappa\nabla^2 T + \alpha_T T_0\frac{\partial p}{\partial t},
\end{aligned} \tag{1}$$

where the pressure (p), temperature (T), and particle velocity ($\vec{v}$) are variables with temporal and spatial dependency. Bulk modulus (B), volumetric expansion coefficient (α_T), density (ρ), first and second viscosity coefficients (λ and μ), specific heat capacity at constant pressure (C_P), thermal conductivity (κ), and ambient temperature (T_0) are constant in each individual layer.

A similar approach can be taken for solid layers, where assuming small deformation, the momentum, and energy conservation equations become (Landau and Lifschitz, 1986b)

$$\begin{aligned}
\rho\frac{\partial^2\vec{u}}{\partial t^2} &= (\lambda_0+\mu_0)\vec{\nabla}(\vec{\nabla}\cdot\vec{u}) + \mu_0\nabla^2\vec{u} + \vec{b}\\
&\quad + (\lambda+\mu)\vec{\nabla}(\vec{\nabla}\cdot\vec{v}) + \mu\nabla^2\vec{v} - \alpha_T B\vec{\nabla}T,\\
\rho C_V\frac{\partial T}{\partial t} &= \kappa\nabla^2 T - \alpha_T B\frac{\partial}{\partial t}\vec{\nabla}\cdot\vec{u}T_0 + S_0.
\end{aligned} \tag{2}$$

This formulation takes into account particle displacement ($\vec{u}$), Lamé elastic coefficients (λ_0 and μ_0) (Salençon, 2001), externally applied body forces ($\vec{b}$), and supplied thermal power density (S_0). Moreover, constant volume specific heat capacity (C_V) is considered in this case.

Assuming plane wave propagation and neglecting external forces, the formulation for both layer types can be rewritten in a one-dimensional manner. Further assuming that the variables p, v, and T are harmonic in the time domain, the partial derivative terms $\partial/\partial t$ and $\partial/\partial x$ can be substituted with $i\omega$ (where ω is the angular frequency of the oscillations) and d/dx, respectively, resulting in a system of ordinary differential equations for each generalized layer, which can be solved to obtain general closed-form solution for each variable (where $\tilde{p} = p - (\lambda+2\mu)dv/dx$),

$$\begin{aligned}
\tilde{p} &= A_j\mathcal{F}(-ik)e^{-ikx} + B_j\mathcal{F}(ik)e^{ikx} + C_j\mathcal{F}(-\sigma)e^{-\sigma x}\\
&\quad + D_j\mathcal{F}(\sigma)e^{\sigma x} + S_j'',\\
v &= A_j\mathcal{G}(-ik)e^{-ikx} + B_j\mathcal{G}(ik)e^{ikx} + C_j\mathcal{G}(-\sigma)e^{-\sigma x}\\
&\quad + D_j\mathcal{G}(\sigma)e^{\sigma x},\\
q &= A_j\kappa ike^{-ikx} - B_j\kappa ike^{ikx} + C_j\kappa e^{-\sigma x} - D_j\kappa e^{\sigma x},\\
T &= A_j e^{-ikx} + B_j e^{ikx} + C_j e^{-\sigma x} + D_j e^{\sigma x} + S_j'.
\end{aligned} \tag{3}$$

A_j, B_j, C_j, and D_j are the integration coefficients that are individual for each layer and are obtained from continuity boundary conditions. The parameters k and σ are the acoustic wavenumber and the thermal attenuation, which can be calculated from

$$k = \pm\frac{\omega}{C_0}\left[1 - \frac{1}{2}\frac{i\omega}{C_0}l_k\left(1-\frac{1}{\gamma}\right) - \frac{1}{2}\frac{i\omega}{C_0}l_V\right] \tag{4}$$

and

$$\sigma = \pm\sqrt{\frac{i\omega\gamma}{C_0 l_k}}\left[1 + \frac{1}{2}\frac{i\omega}{C_0}l_k\left(1-\frac{1}{\gamma}\right) + \frac{1}{2}\frac{i\omega}{C_0}l_V(1-\gamma)\right], \tag{5}$$

where l_k and l_V are characteristic lengths associated with conduction and viscous processes,

https://doi.org/10.1121/10.0017598

$$l_k = \frac{C_0\kappa}{BC_P}, \quad l_V = \frac{\lambda + 2\mu}{\rho C_0}, \tag{6}$$

and $C_0 = \sqrt{B\gamma/\rho}$. The functions $\mathcal{F}(\xi)$ and $\mathcal{G}(\xi)$ are described as

$$\mathcal{F}(\xi) = \alpha_T B - \left(\frac{B}{i\omega} + \lambda + 2\mu\right)\left(L_1\xi^2 + L_2\xi^4\right),$$
$$\mathcal{G}(\xi) = L_1\xi + L_2\xi^3, \tag{7}$$

where the terms L_1 and L_2 are

$$L_1 = -\frac{1}{i\omega\rho}\left[\alpha_T B + \frac{i\omega\rho C_V}{\alpha_T T_0 B}\left(\lambda + 2\mu - \frac{iB}{\omega}\right)\right],$$
$$L_2 = \left(\lambda + 2\mu - \frac{iB}{\omega}\right)\frac{\kappa}{i\omega\rho\alpha_T T_0 B}. \tag{8}$$

The terms S_j' and S_j'' represent the supplied thermal power

$$S_j' = \frac{S_0}{i\omega\rho C_V}, \quad S_j'' = \alpha_T B S_j', \tag{9}$$

and appear only in layers of solid. The full steps needed to reach the closed-form solution [Eqs. (3)–(9)] are described in detail in Guiraud *et al.* (2019a).

For a given N-layered thermophone structure, the obtained set of solutions can be conveniently written in matrix form, valid for any layer j within the structure,

$$\begin{bmatrix} \tilde{p} \\ v \\ q \\ T \end{bmatrix}_j = H_j(x)\begin{bmatrix} A_j \\ B_j \\ C_j \\ D_j \end{bmatrix} + \begin{bmatrix} S_j'' \\ 0 \\ 0 \\ S_j' \end{bmatrix}, \tag{10}$$

where

$$H_j(x) = \begin{bmatrix} \mathcal{F}(-ik) & \mathcal{F}(ik) & \mathcal{F}(-\sigma) & \mathcal{F}(\sigma) \\ \mathcal{G}(-ik) & \mathcal{G}(ik) & \mathcal{G}(-\sigma) & \mathcal{G}(\sigma) \\ \kappa ik & -\kappa ik & \kappa\sigma & -\kappa\sigma \\ 1 & 1 & 1 & 1 \end{bmatrix} \times \begin{bmatrix} e^{-ikx} & 0 & 0 & 0 \\ 0 & e^{ikx} & 0 & 0 \\ 0 & 0 & e^{-\sigma x} & 0 \\ 0 & 0 & 0 & e^{\sigma x} \end{bmatrix}. \tag{11}$$

The constants A_j, B_j, C_j and D_j can be obtained from continuity between two adjacent layers. After resolving the pressure field on the surface of the thermo-acoustic emitter, the far field acoustic pressure is calculated from the superposition of surface points (such that each point is considered as an acoustic source) using Rayleigh's second integral,

$$p_{FF}(x,y,z) = \frac{i\omega\rho_g}{4\pi}\int_{-L_y}^{L_y}\int_{-L_z}^{L_z} v(y',z') \times \frac{e^{-ik_g\sqrt{(x-x_0)^2+(y-y')^2+(z-z')^2}}}{\sqrt{(x-x_0)^2+(y-y')^2+(z-z')^2}} \times dz'dy', \tag{12}$$

where v is the surface velocity, $(-L_y, L_y) \times (-L_z, L_z)$ are the dimensions of the thermophone surface, x, y, and z are the coordinates of the observation point and x_0, y', and z' are the coordinates of generation points. The thermophone's thermal efficiency can then be calculated via

$$\eta_{th} = \underbrace{\frac{q_{th} + q_{sub}}{P_{in}}}_{a_1} \cdot \underbrace{\frac{q_{th}}{q_{th} + q_{sub}}}_{a_2}, \tag{13}$$

where q_{th} and q_{sub} are the heat fluxes through thermophone and substrate layers, respectively, and P_{in} is the total supplied thermal power. This formulation takes into account the consumed portion of supplied thermal power that generates oscillating heat flux at the thermophone boundary (term a_1) and the fluctuating power split between the solid layers according to the thermal product ratio (term a_2). The present approach is consistent with prior effort of the authors ($\eta(\omega)$ term of Eq. (8) from Julius *et al.* (2018), and while it only describes the efficiency of generated surface heat flux oscillations, it can be multiplied by additional frequency-dependent terms to also account for the acoustic efficiency. In the scope of the present paper, the acoustic efficiency is not considered and η_{th} is used directly as the figure of merit towards evaluation of the more favorable thermophone properties.

B. Thermo-acoustic simulation

The solutions for each variable are now fully described and can serve as a basis for a generalized simulation framework geared towards estimating the performance of multi-layered thermo-acoustic emitter designs. The simulation is structured to receive an input of relevant experimental conditions—thermo-acoustic emission area, ambient temperature in the surrounding fluid, range of evaluated frequencies, and location of microphone sensor with respect to the emitting surface. In the following, the simulation is supplied with an array containing sets of N-layered thermophone designs, which are described by their layer-by-layer composition. Each thermophone layer is defined in terms of its domain type (fluid, thermophone solid–active excitation source, or substrate solid), thickness, density, bulk modulus, specific heat, thermal conductivity, coefficient of thermal expansion, and Lamé viscosity parameters. Supplied power is also added at this stage in the relevant layers.

Having fully defined the simulated thermophone structure, the program solves propagation from the generating layer toward external boundaries and subsequent conversion of thermal energy into acoustic waves, based on the

thermophone performance model. At first, the various parameters are obtained in each layer. Then, the solver resolves the continuity requirement at the layer-to-layer interfaces. Finally, the code calculates acoustic propagation through the layers and estimates the efficiency of the thermo-acoustic process. The outputs of the simulation include thermal, acoustic, and total efficiencies, generated far- and near-field pressures, and additional auxiliary information (such as temperature, velocity, pressure, and heat-flux distributions).

Since different emitter architectures or applied excitation frequencies can be solved independently, the algorithm relies on parallel computing to reduce calculation time through simultaneous evaluation of numerous thermophone designs or estimation of acoustic generation at various frequencies. In this case, the solver uses a single program multiple data approach (Sterling *et al.*, 2018)—the same instructions are performed by several computer cores in parallel over different input data sets. Since the simulation is of strong scaling type (the size of the original problem does not change with an increasing number of cores), Amdahl's law (Gustafson, 1988) can be implemented to estimate the associated speedup,

$$SP = \frac{1}{1 - f_p + \frac{f_p}{g}}, \tag{14}$$

where f_p is the code portion that can be parallelized, g is the available number of cores, and SP is the speedup ratio (single core time-to-solution with respect to multi-core time-to-solution). Since ∼5% of the simulation is dedicated to the preparation of the input arrays and other data management tasks, the parallel portion of the code is ∼0.95. Using standard 4- and 8-core CPUs, the simulation speedup ratio is ∼3.5 and ∼6, respectively.

C. Simulated cases

The effects associated with various properties of the thermo-acoustic emitter structure are analyzed by introducing a generic thermophone architecture with parameterized layer features. This generalized design, illustrated in Fig. 1, is comprised of a semi-infinite baseplate, insulating substrate layer, actuated thermophone film, and semi-infinite expanse of air. The properties of the top and bottom layers are kept constant, whereas the parameters of the thermophone and substrate are variated in the scope of the study. The checked variables include thickness (L), density (ρ), specific heat capacity (C_P), and thermal conductivity (κ) for the two parametrized layers. The simulated variable ranges, summarized in Table I, are selected to match the typical material properties of metallic thermophones and ceramic substrates (in terms of density, specific heat capacity, and thermal conductivity), and the capabilities of common thin-film fabrication methods (in terms of layer thickness). Each of the eight variables is checked at four distinct points within its range, distributed with logarithmic spacing. This results in a simulation space that includes 65 536 unique thermophone designs. For the sake of completing the simulation input requirements, the top layer is always described using the relevant properties of air, whereas the baseplate is modelled as a semi-infinite slab of titanium in every simulated case. Towards enabling comparison between the obtained results, all cases are solved at a constant power input of 200 [W] in the frequency range from 1 to 15 [kHz]. Since all thermo-acoustic efficiency results indicate similar behavior, the figures that depict the findings of simulations are presented at 1 [kHz] for the sake of brevity.

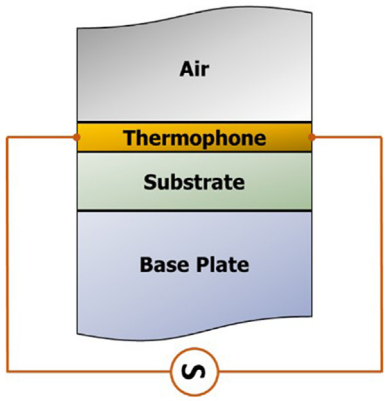

FIG. 1. (Color online) Generalized thermophone structure composed of semi-infinite baseplate, insulating substrate, active thermophone film, and semi-infinite layer of air.

III. EXPERIMENTAL METHODOLOGY

A. Experimental facility

The simulation findings are validated in a purpose-built measurement facility, represented schematically in Fig. 2. The setup includes a small anechoic chamber, where the emitters are placed during experiments, range of sensors and data acquisition tools, and a circuit that generates required electric excitation.

The thermo-acoustic transducers are powered by a sine signal that is produced by Tektronix AFG3102 function generator (Tektronix, Beaverton, OR) and amplified using PKN Audio XE10000 10 [kW] dual-channel amplifier (PKN Audio Ltd., Szekesfehervar, Hungary). Since the amplifier is designed to power typical audio equipment with an impedance range from 2 to 16 [Ω], while the typical resistance of the thermo-acoustic sources varies between 0.4 and 1.5 [Ω], the power loop also includes a 100 [W] variable shunt resistor that produces complementary load based on per-experiment requirements.

TABLE I. Summary of simulated variable ranges.

Layer	Variable	Range	Units
Thermophone	L	$40 \cdot 10^{-9}$–$5 \cdot 10^{-4}$	[m]
	ρ	$3 \cdot 10^{3}$–$21 \cdot 10^{3}$	[kg/m^3]
	C_P	50–700	[J/kgK]
	κ	30–400	[W/mK]
Substrate	L	$5 \cdot 10^{-6}$–$5 \cdot 10^{-4}$	[m]
	ρ	$0.2 \cdot 10^{3}$–$5 \cdot 10^{3}$	[kg/m^3]
	C_P	30–1000	[J/kgK]
	κ	0.3 – 3	[W/mK]

https://doi.org/10.1121/10.0017598

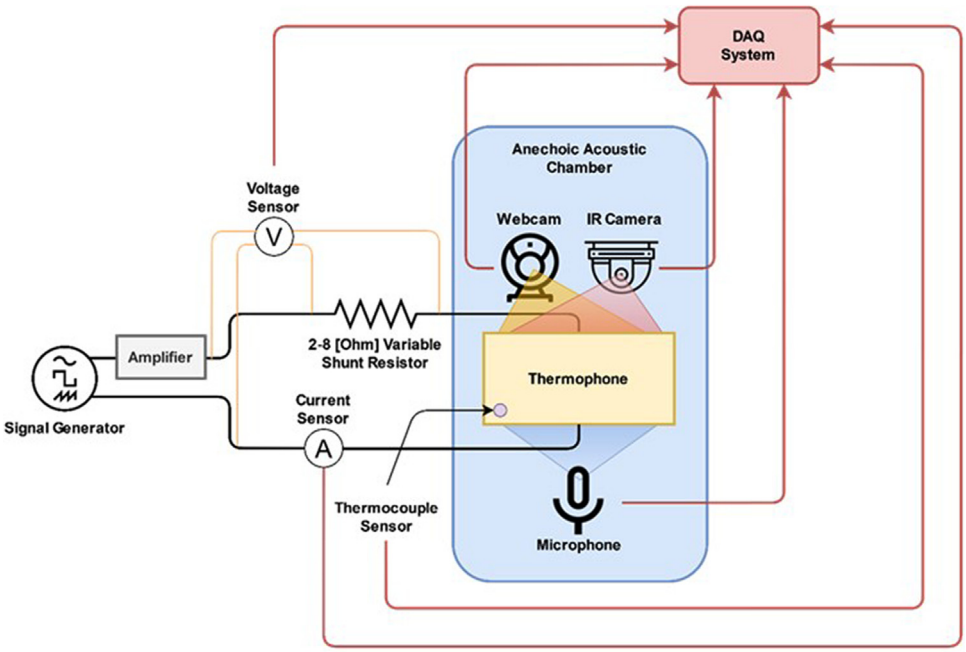

FIG. 2. (Color online) Schematic of the thermo-acoustic test facility.

The delivered power is evaluated via measurements of instantaneous voltages and currents. Thermophone voltage is obtained by differential voltage measurement (subtraction of voltage drop across the shunt from the voltage drop across the shunt and the thermophone), recorded by a NI-9215 analogue voltage acquisition module, whereas the current is obtained by Riedon SSA-100 (Riedon, Alhambra, CA) current sensor, which generates a voltage signal of 12.5 [mV] per each 1 [A] and is sampled using the same voltage acquisition device. The acoustic output is measured with a GRAS 40BE pre-polarized free-field condenser microphone (GRAS Sound & Vibration, Holte, Denmark), amplified via GRAS 26CB-HT pre-amplifier and Endevco 133 signal conditioner (Endevco, San Juan Capistrano, CA), and sampled with a NI-9223 high-speed voltage acquisition module and Tektronix TDS2004C digital oscilloscope (Tektronix, Beaverton, OR).

To monitor the measured thermo-acoustic device, the facility is equipped with a set of two cameras that produce video output in visual and infrared spectra (Logitech C270 HD webcam; Logitech, Lausanne, Switzerland; and Optris Xi 400, Optris, Berlin, Germarny, respectively), and with a K-type thermocouple, that measures the temperature of the sample backing and which is recorded via NI-9211 thermocouple acquisition module. All data acquisition modules transmit sampled data via NI cDAQ-9185 4-channel chassis, which is controlled by LabVIEW. The measurements are subsequently post-processed in MATLAB to obtain relevant parameters.

B. Experimental samples

Validation of simulation findings is done using a set of experimental samples that mimic the change in substrate and thermophone layers' parameters and enable the comparison of their actual performance impact with the simulated trends. The general schematic of the manufactured 4-layered thermo-acoustic devices is presented in Fig. 3.

The active area of the thermophone layer is 10×10 [mm]. The thermophone and substrate layers are produced at two different thicknesses 200 and 1000 [nm], and 5 and 10 [μm], respectively, whereas the base slab is a $30 \times 30 \times 1.75$ [mm] plate of titanium. In this case, an additional bonding layer is required between the thermophone and the substrate to improve their adhesion, which consists of 40 [nm]-thick layer of titanium.

The manufacturing process of each sample involves several distinct steps. First, the surface of the base layer is treated to enable subsequent deposition on the substrate. Then, the substrate, bonding, and thermophone layers are deposited via various vacuum coating processes. Thin layer deposition techniques are common in the integrated circuit industry, where they are used to create electronic circuits on top of semiconductor material. In this application, the base is typically a silicon wafer that has a root mean square (RMS) surface roughness (R_q) of ≤ 1 [Å] (Teichert *et al.*, 1995). Since vacuum deposition methods produce coatings based on their line of sight, this surface finish yields highly

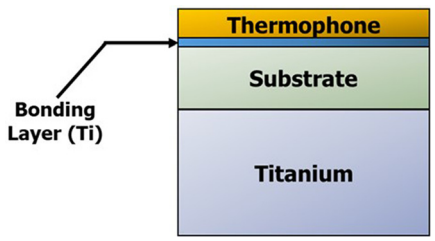

FIG. 3. (Color online) General schematic of manufactured thermophone test samples.

uniform layers. However, in the case of the present effort, the base is a coarse plate of titanium and therefore, its surface quality needs to be significantly improved prior to deposition.

Towards enhancing the surface finish of the titanium base layers, the employed surface treatment method involves using a high-precision polishing machine (ATM Saphir 520, ATM Qness GmbH, Mammelzen, Germany) with a range of ultra-high grit polishing compounds. The quality of the representative polished surfaces is measured with a KLA-Tencor Alpha-Step 500 (KLA Corporation, Milpitas, CA) stylus-type profilometer (sampling length of 500 $[\mu m]$ with a sub-angstrom vertical resolution). The surface qualities are obtained in terms of the arithmetical mean deviation of the assessed profile (R_a),

$$R_a = \frac{1}{l_r}\int_0^{l_r} |z(x)|dx, \tag{15}$$

where l_r is the sampling length and $z(x)$ is the surface profile distribution along the sampling path ($R_q \approx 1.1R_a$). The obtained characteristic surface roughness is $R_a = 135.8\,[\text{Å}]$.

The materials selected for creating the thermophone layer in the test specimens include gold, platinum, palladium and ruthenium, while the tested substrates are silicon dioxide and silicon nitride. The properties of all used materials are summarized in Table II in terms of density, specific heat capacity, and thermal conductivity. Since each material is checked at two different thicknesses and in all possible permutations, the overall experimental space contains a total of 32 combinations.

In the scope of this paper, both ceramic materials used as thermophone substrates (SiO_2 and Si_3N_4) are deposited via Plasma-Enhanced Chemical Vapor Deposition (PECVD) technique, whereas the bonding and thermophone layers are manufactured via Physical Vapor Deposition (PVD). The SiO_2 and Si_3N_4 substrate layers are deposited at 573 [K] using mixtures of silane gas (SiH_4) and nitrous oxide (N_2O) or ammonia (NH_3), respectively. The deposition times for each 5 $[\mu m]$ cycle are 51 [min] (SiO_2) and 210 [min] (Si_3N_4). The pressures in the chamber are kept at 187 [Pa] and 120 [Pa] for SiO_2 and Si_3N_4, respectively. The active metallic layers are produced using e-beam evaporation (gold) and magnetron sputtering (platinum, palladium, and ruthenium). In each case, the bonding titanium layer is deposited using the same method as the thermophone above it. In the case of

TABLE II. Properties of the selected thermophone and substrate layer materials.

Layer	Material	$\rho\,[\text{kg/m}^3]$	$C_P\,[\text{J/kgK}]$	$\kappa\,[\text{W/mK}]$
Thermophone	Gold (Au)	19 300	130	312
	Platinum (Pt)	21 460	132	71
	Palladium (Pd)	12 025	245	73.5
	Ruthenium (Ru)	12 300	235	113.5
Substrate	Silicon dioxide (SiO_2)	2 410	705	1.4
	Silicon nitride (Si_3N_4)	2 810	886.5	26.5

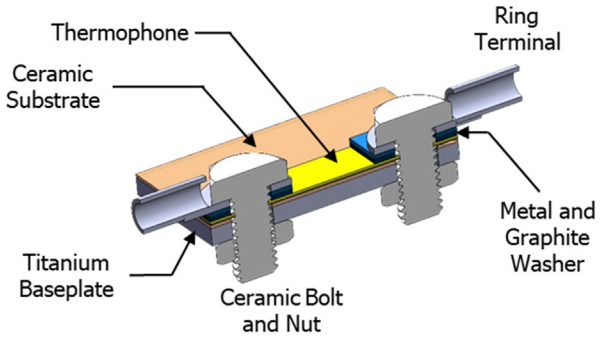

FIG. 4. (Color online) Cross-section of the fully assembled thermo-acoustic source.

e-beam evaporation, the sample distance is 500 [mm], the deposition rate is 3 $[\text{Å}/s]$ and the base pressure is $5.5 \cdot 10^{-7}$ [Pa]. In the case of magnetron sputtering, the working distance is 100 [mm], the chamber pressure is 0.3 [Pa], the magnetron power is 200 [W], the flow rate of argon is 45 [sccm] and the deposition rate is 1.7 $[\text{Å}/s]$. Moreover, while the substrate is kept unheated in majority of cases, during deposition of ruthenium, the substrate is heated to 373 [K].

The final manufacturing step is the attachment of input terminals that are used to supply the thermophone with electric power during the experiments. The implemented concept involves ring terminal connectors, which are fastened to the thermo-acoustic emitter with ceramic bolts and nuts (Fig. 4). The connectivity between the terminals and the active layer is further enhanced by twin-layered metal and graphite washer. Some examples of produced thermoacoustic devices are presented in Fig. 5, where it can be noted that the yellowish hue in the background is indicative of Si_3N_4 substrate, whereas the gray color is typical of a layer of SiO_2.

C. Experimental procedure

The developed facility is used to measure the performance of all manufactured thermo-acoustic sources with an RMS power input of 2, 4, and 6 [W]. These power levels enable prolonged stable thermophone operation at lower temperatures, while preventing oxidation and damage to the thermo-acoustic device. However, they also require a relatively close microphone placement to record a sufficient acoustic signal. Yet, since the thermo-acoustic devices are inherently distributed sources that simultaneously generate sound from each point on their surface, placing the

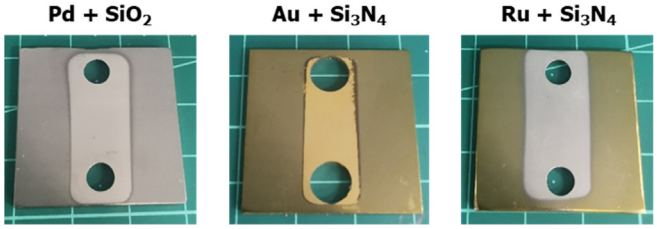

FIG. 5. (Color online) Examples of produced samples (color online).

https://doi.org/10.1121/10.0017598

microphone too close to them would result in measurement inaccuracies due to interactions between various points on the plane. Thus, the microphone should be placed at a distance that allows it to measure the thermo-acoustic emission as if it originates from a monopole source.

This distance is evaluated via the approach suggested in Bies *et al.* (2018) for estimating the relative level of a rectangular source compared to a monopole. On the axis of symmetry, the maximal mean square sound pressure from a rectangular planar source is

$$\langle p^2 \rangle = \frac{2\rho c W}{\pi HL} \cdot \tan^{-1}\left[\frac{HL}{2r\sqrt{H^2+L^2+4r^2}}\right], \tag{16}$$

where c is the speed of sound, W is the radiated sound power, H and L are the source dimensions, and r is the observation distance. In the case of monopole, the equation reduces to

$$\langle p^2 \rangle = \frac{\rho c W}{2\pi r^2}. \tag{17}$$

The level of the rectangular source can be compared to baseline monopole by defining normalized distance ($r/\sqrt{HL}$) and α-ratio ($\alpha = H/L$ if $L < H$, or $\alpha = L/H$ if $L > H$) terms. In the present case, where $L = H$ and $\alpha = 1$, a normalized distance of ~3.5 is sufficient to obtain the same signals. The microphone is therefore placed with a sufficient factor of safety at a distance of 75 [mm] above the active thermophone layer along the central axis and is kept static during the entire duration of the experimental campaign.

The measured frequency ranges are then determined from the limitations of the experimental setup. The higher limit is selected as 15 [kHz], which is within the upper linearity range of the used amplifier. The lower limit is the lowest frequency that enables the microphone to still measure the signal in the far field. This threshold can be estimated by satisfying three criteria (Bies, 1976),

$$r \gg \frac{\lambda}{2\pi}, \quad r \gg l, \quad r \gg \frac{\pi l^2}{2\lambda}, \tag{18}$$

where λ is the wavelength of radiated sounds and l is the characteristic dimension of the source. The "much greater than" criterion in the previously noted expressions refers to a factor of three or more. Adhering to an even more stringent approximation of far field being at the distance of at least a single wavelength (MacDonald, 2020), the lower frequency limit is selected as 5 [kHz]. Then, the data is acquired within the tested 5–15 [kHz] range with a 1 [kHz] step. Thirty seconds of data are recorded at each point with a sampling frequency of 100 [kS/s]. The control application stores the acquired signals in time domain and they are post-processed in MATLAB to obtain acoustic performance (in terms of pressure p [Pa]) and performance characteristic, which is indicative of the efficiency (in terms of measured pressure per unit of delivered power p/PW [Pa/W]). Although another performance metric of acoustic efficiency was suggested in the prior literature (Vesterinen *et al.*, 2010), it has a linear dependency on input power, thereby creating a bias towards thermo-acoustic devices with higher power inputs. Instead, the presently suggested p/PW parameter is power invariant and is therefore better suited to comparatively analyze the performance of thermo-acoustic variables with varying power input.

The uncertainties of the reported findings are evaluated according to a standard methodology suggested by the National Institute of Standards and Technology (Taylor and Kuyatt, 1994). According to this approach, the maximal errors in the calculations of acoustic pressure and performance characteristic are ±30% and ±15%, respectively.

IV. RESULTS

A. Thermophone simulation

The simulation dataset results for the variated thermophone architectures are studied using multi-way analysis of variance method. This data comparison approach is commonly used to study the effects of individual factors and their joint contributions on the mean of results in large multi-parametric datasets. Using this method, the observed variance in a particular set of measurements is partitioned into components attributable to different sources. This technique then yields a set of quantitative values (one per variation term) by testing the effects of multiple individual factors and their joint contribution on the mean of given results vector (Galbraith *et al.*, 1975).

In the case of the present effort, the eight varied parameters (thickness, density, specific heat capacity, and thermal conductivity of the thermophone and the substrate layers) become the factors of variance analysis. Hence, their relative importance is analyzed by looking at their effect on the mean thermal efficiency (η_{th}) using F-test over a full factorial logarithmically spaced population. The relative importance of the main factors (as obtained from the F-test analysis) is summarized along with the gradient and limit of their effect in Table III with a confidence interval of 95%. Compared to these terms, first- and higher-order interactions between the individual parameters are found to be negligible

TABLE III. Relative importance of the thermophone and substrate layers' parameters and their effect on the mean total efficiency.

Layer	Variable	Importance	Effect Gradient	Limit
Thermophone	L	24 845	$L_{th} \uparrow \rightarrow \eta_{tot} \downarrow$	Min. limit of ~500 [nm]
	ρ	587.2	$\rho_{th} \uparrow \rightarrow \eta_{tot} \downarrow$	No limit
	C_P	1081	$C_{Pth} \uparrow \rightarrow \eta_{tot} \downarrow$	No limit
	κ	0.01	No effect	No limit
Substrate	L	5716	$L_{sub} \uparrow \rightarrow \eta_{tot} \uparrow$	Max. limit of ~100 [μm]
	ρ	3898	$\rho_{sub} \uparrow \rightarrow \eta_{tot} \downarrow$	No limit
	C_P	4634	$C_{Psub} \uparrow \rightarrow \eta_{tot} \downarrow$	No limit
	κ	11 622	$\kappa_{sub} \uparrow \rightarrow \eta_{tot} \downarrow$	No limit

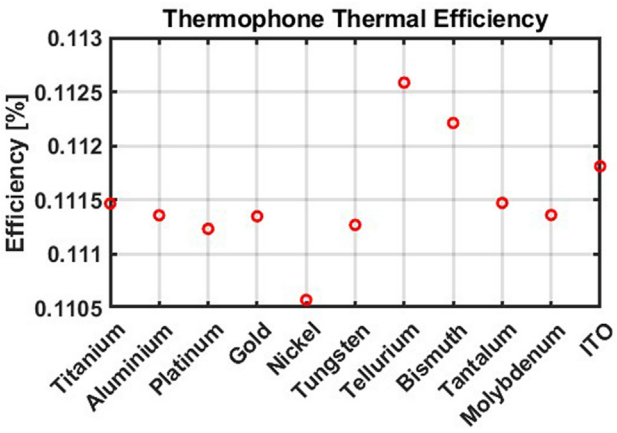

FIG. 6. (Color online) Performance of various 200 [nm]-thick thermophone layers placed on a 10 [μm]-thick layer of SiO_2.

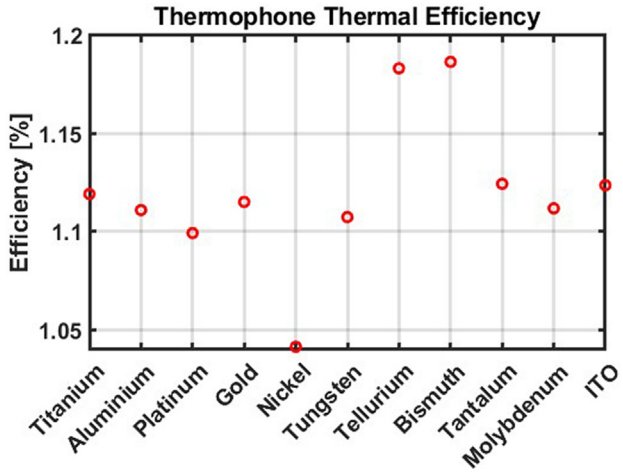

FIG. 7. (Color online) Performance of various 200 [nm]-thick thermophone layers placed on a 10 [μm]-thick layer of Silica Aerogel.

(at least an order of magnitude lower) and are therefore omitted from further analysis.

Interestingly, an increase in almost all variable property values is shown to be detrimental to the device performance, with the only exception being substrate thickness, where thicker layer results in higher efficiency. The results suggest that the parameters with the largest impact on the thermo-acoustic performance are the thicknesses of the two layers and the thermal conductivity of the substrate. However, the thermal conductivity of the thermophone has no effect on the efficiency in the case of the presently discussed supported film designs. As a matter of fact, it can be observed that beyond its thickness, the thermophone layer has a very limited influence on the thermo-acoustic emission. This effect can be better showcased by conducting a complementary set of simulations using properties of real materials. This analysis is charted in Figs. 6 and 7 where different 200 [nm]-thick thermophones with wide range of properties (titanium, aluminum, platinum, gold, nickel, tungsten, tellurium, bismuth, tantalum, molybdenum, and indium tin oxide) are simulated on 10 [μm]-thick Silicon Dioxide (SiO_2) and Silica Aerogel substrates, respectively. Although there is an order of magnitude shift between the means of the two datasets associated with the change in substrate thermal conductivity (1.4 [W/mK] for SiO_2 and 0.017 [W/mK] for Silica Aerogel), the performances of individual models within each set are comparable to each other. This is also indicated by the low coefficient of variation (ratio between the standard deviation and the mean of each dataset) value obtained in both cases—0.5% and 3.5% for SiO_2 and Silica Aerogel, respectively.

An additional conclusion can be made regarding the bounds of effect—in the case of densities, specific heat capacities, and thermal conductivities, the effect does not exhibit diminishing returns within the tested range (the rates of variables' decreases and efficiency increase are similar). An example of this is presented in Fig. 8 (left), where the

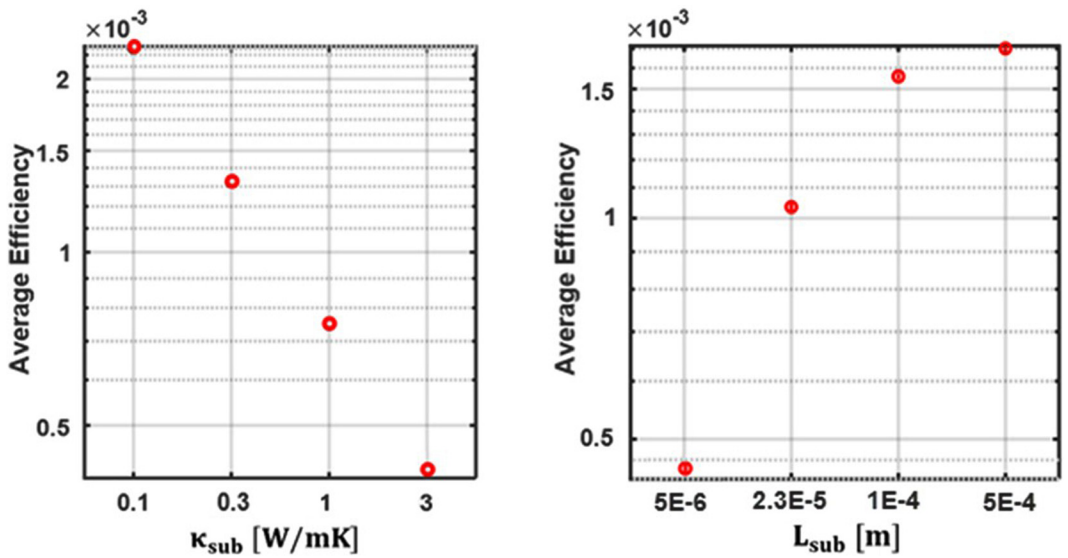

FIG. 8. (Color online) Impact of change in substrate thermal conductivity (left) and in substrate thickness (right) on the average efficiency of all thermophone designs with a given value of κ_{sub} or of L_{sub}.

https://doi.org/10.1121/10.0017598

average efficiency of all samples with a given value of substrate thermal conductivity is charted against κ_{sub} on a logarithmic scale. The data in the figure suggests that, within the simulated range, the change in the value of κ_{sub} has an ongoing effect that alters the thermo-acoustic efficiency at a constant rate. However, in the case of thicknesses, there is a distinct limit beyond which the impact on the efficiency is severely reduced ($L_{th} \lesssim 500$ [nm] and $L_{sub} \gtrsim 100$ [μm]). This effect is demonstrated in Fig. 8 (right), which charts the impact of change in L_{sub} and where diminishing influence can be observed at higher substrate layer thicknesses.

B. Experimental measurements

Simulation results can now be compared with the findings of the experimental campaign. The gamut of tested designs enables the validation of the effects associated with the three most dominant properties (thicknesses of the layers and thermal conductivity of the substrate), as well as to experimentally demonstrate the minor relevance of thermophone layer material. To analyze the effects associated with the thermophone layer (thickness and thermal conductivity), different thermophone materials can be studied using the same representative substrate. This analysis is represented in Fig. 9, where the thermophone's performance characteristic (in terms of [Pa/W]) is charted against frequency (in [kHz]). Points' colors stand for the different thermophone materials (gold–blue points, palladium–red points, platinum–yellow points, and ruthenium–purple points), whereas the points' shape signifies the thermophone layer thickness (stars for 200 [nm]-thick thermophones and circles for 1000 [nm]-thick thermophones). The representative substrate is a 10 [μm]-thick layer of silicon dioxide. The points are obtained by averaging efficiencies from three power inputs (2, 4, and 6 [W]), which are observed to collapse onto a single value within 7%, thereby validating the power invariability assumption for the p/PW performance parameter.

These results are in good agreement with the simulation findings and indicate that, in the case of supported thermo-acoustic layers, the thermophone material has a limited impact on the thermo-acoustic performance at lower frequencies or higher thickness (given the same thickness of the compared layers), whereas the layer thickness has a much more prominent impact on performance: thinner thermophones outperform their thicker counterparts.

The effects associated with the substrate thickness and thermal conductivity can be studied in a similar manner by looking at the performance of representative thermophone layers on different substrates. This data is charted in Fig. 10, where the points' colors stand for the different substrate materials (silicon dioxide, red points; silicon nitride, blue points), whereas the points' shape signifies the substrate layer thickness (circles for 5 [μm]-thick substrates and stars for 10 [μm]-thick substrates). The representative thermophone is a 200 [nm]-thick layer of gold.

The obtained results describe the impact of the substrate thermal conductivity, which is indicated by the shift between the differently colored points, and the impact of the substrate thickness, which is demonstrated by the difference between the circular and the star-shaped points of the same color. As predicted by the simulations, the substrate with lower thermal conductivity (silicon dioxide) indeed has a generally superior performance. Moreover, thicker substrates (star-shaped points) also outperform their thinner counterpart, thereby further corroborating the conclusions of the simulation campaign. It is interesting to note that, in this case, although doubling of the silicon nitride layer has a clearly visible effect, in general, it still results in a performance comparable to a thinner coating of silicon dioxide. Similar trends can also be observed in other tested thermo-acoustic devices.

Beyond investigating the trends, experimentally measured pressure levels can also be directly compared to model predictions by conducting additional simulations after updating the simulated architecture to include the additional bonding layer and the actual physical properties and dimensions of the manufactured units. Therefore, updated simulations are conducted in the frequency range from 5 to 15 [kHz] for all tested materials and the results are compared with the experimental findings. In the following, the deviations between the experimentally observed and the

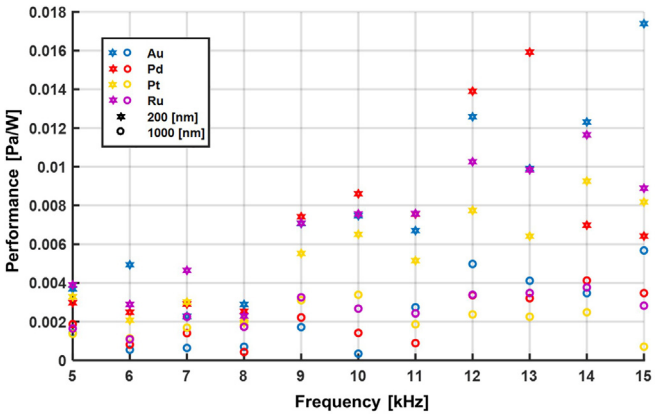

FIG. 9. (Color online) Performance characteristic of various thermophone layers on a representative 10 [μm]-thick silicon dioxide substrate layer.

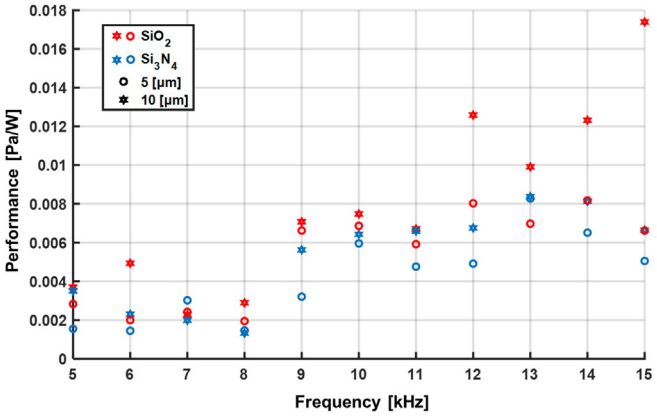

FIG. 10. (Color online) Performance characteristic of representative 200 [nm]-thick golden thermophone layers on various substrates.

TABLE IV. Absolute mean deviations between the measured and the simulated pressures within tested range from 5 to 15 [kHz].

			Thermophones							
			Au		Pd		Pt		Ru	
			200 [nm]	1000 [nm]	200 [nm]	1000 [nm]	200 [nm]	1000 [nm]	200 [nm]	1000 [nm]
Substrates	SiO_2	5 [μm]	4%	12%	7%	3%	13%	8%	1%	N/A
		10 [μm]	6%	7%	4%	13%	4%	6%	7%	6%
	Si_3N_4	5 [μm]	24%	11%	24%	11%	22%	12%	26%	17%
		10 [μm]	22%	2%	20%	6%	22%	9%	28%	20%

calculated values are averaged across measured ranges of frequencies (from 5 to 15 [kHz]) and powers (2, 4, and 6 [W]) for each produced sample. The results of this comparison are summarized in Table IV. One of the thermo-acoustic emitters (1000 [nm]-thick layer of ruthenium on 5 [μm]-thick silicon dioxide substrate) was observed to have surface defects after manufacturing, and it is therefore absent from this comparison. Overall, the results of the experiments are found to be well-matched by the numerical model in this diverse set of designs.

V. DISCUSSION AND SUMMARY

The results of the experimental campaign fully corroborate the simulation's prediction and indicate that the variables that have the strongest impact on the thermo-acoustic performance are the thicknesses of the substrate and thermophone layers, i.e., thicker substrates and thinner thermophones have superior characteristics with respect to their counterparts. Considering that the substrate thermal conductivity is typically significantly lower than the thermophone's one, these findings have an intuitive explanation. The substrate limits the heat flux from the thermophone backing and the heat instead emanates into the surrounding media where it is converted into pressure oscillations. Therefore, thicker substrates serve as an even better thermal insulator. At the same time, since thermo-acoustic phenomena occur at the boundary between the solid and the fluid layers, any heating that occurs inside the thermophone layer cannot be converted to pressure. Thus, thinner thermophones have a larger proportion of surface heating and are generally less lossy.

An additional important parameter is the thermal conductivity of the substrate, which adheres to the same reasoning—lower thermal conductivity provides superior insulation properties and yields improved thermo-acoustic performance. However, for supported films, the thermal conductivity of the thermophone has a limited effect within the tested ranges of variables. This can be in part explained by an order of magnitude difference between the thicknesses of the two layers and the results might differ for designs with significantly thicker thermophone layer. As a matter of fact, in the scope of this study, beyond its thickness, the composition of the thermophone layer has a diminished influence on the final performance, as indicated by simulations and measurements of different equally thick thermophones on the same substrate (particularly at higher thermophone thicknesses). However, as present work is only concerned with Fourier conduction as the means to propagate heat flux through solid media, perhaps future thermophones that leverage non-Fourier conduction effects would exhibit greater dependency on material properties.

Finally, the experimental results are directly comparable with the simulation predictions and the deviation between the two values is within the limits of the experimental accuracy. Higher deviations are consistently observed in the case of silicon nitride substrate. This discrepancy can be attributed to the relatively large range of typical thermal conductivity values for silicon nitride (10–43 [W/mK]) (AZO Materials, 2022). Although the simulations conducted in the scope of the present effort are all supplied with a single bulk value (Table II), the actual thermal conductivity of the substrate layers of the samples used in the experimental campaign could be different. This observation can be contrasted with the comparison results for the samples with silicone dioxide substrates since in sufficiently thick layers, with thickness of above 200 [nm], the thermal conductivity matches the bulk value (Lasance, 2004), and the experimental findings are significantly better matched with the numerical predictions.

Overall, these findings provide an insight into the effect of evaluated properties and offer a set of tangible experimentally validated guidelines that can be applied in the future to produce higher-efficiency thermophone-on-substrate thermo-acoustic emitters. Moreover, the developed simulation framework can be readily implemented as a robust tool for the development and design optimization of other advanced multi-layered thermophone devices. Although the present effort focuses on principal trends toward efficient multi-film designs, future works could potentially focus on complex configurations, such as foam-like and porous thermo-acoustic sources. Instead of relying on the multi-layer approach implemented in the scope of the present paper, these advanced geometries would require a different model, such as the one described in Guiraud *et al.* (2019b). These three-dimensional sources can potentially be capable of benefiting from dramatic efficiency improvements, typical to free-standing thermophone designs. Since modern free-standing designs seldom have practical applications due to their fragility, these robust porous designs could pave the wave toward future implementation in various acoustic systems.

https://doi.org/10.1121/10.0017598

ACKNOWLEDGMENTS

This present research effort has received funding from the European Research Council (ERC) under the European Union's Horizon 2020 Research and Innovation Programme (Grant Agreement No 853096, ThermoTON). It was also partially supported by Israel Science Foundation (Contract No. 999/19).

Aliev, A. E., Codoluto, D., Baughman, R. H., Ovalle-Robles, R., Inoue, K., Romanov, S. A., Nasibulin, A. G., Kumar, P., Priya, S., Mayo, N. K., and Blottman, J. B. (**2018**). "Thermoacoustic sound projector: Exceeding the fundamental efficiency of carbon nanotubes," Nanotechnol. **29**(32), 325704.

Aliev, A. E., Gartstein, Y. N., and Baughman, R. H. (**2013**). "Increasing the efficiency of thermoacoustic carbon nanotube sound projectors," Nanotechnology **24**(23), 235501.

Aliev, A. E., Lima, M. D., Fang, S., and Baughman, R. H. (**2010**). "Underwater sound generation using carbon nanotube projectors," Nano Lett. **10**(7), 2374–2380.

Arnold, H. D., and Crandall, I. B. (**1917**). "The thermophone as a precision source of sound," Phys. Rev. **10**(1), 22–38.

AZO Materials (**2022**). "Silicon nitride (Si3N4) properties and applications," https://www.azom.com/properties.aspx?ArticleID=53 (Last viewed February 14, 2023).

Barnard, A. R., Jenkins, D. M., Brungart, T. A., McDevitt, T. M., and Kline, B. L. (**2013**). "Feasibility of a high-powered carbon nanotube thin-film loudspeaker," J. Acoust. Soc. Am. **134**(3), EL276–EL281.

Bies, D., Hansen, C., and Howard, C. (**2018**). *Engineering Noise Control*, 5th ed. (CRC Press, Boca Raton, FL).

Bies, D. A. (**1976**). "Uses of anechoic and reverberant rooms," Noise Control Eng. **7**, 154–163.

Boullosa, R. R., and Santillan, A. O. (**2004**). "Ultrasound radiation from simple thermoacoustic transducers," Acta Acust. united Ac. **90**(2), 277–284.

Bouman, T. M., Barnard, A. R., and Asgarisabet, M. (**2016**). "Experimental quantification of the true efficiency of carbon nanotube thin-film thermophones," J. Acoust. Soc. Am. **139**(3), 1353–1363.

Braun, F. (**1898**). "Notiz über Thermophonie" ("Note on thermophony"), Ann. Phys. **301**(6), 358–360.

Brown, J. J., Moore, N. C., Supekar, O. D., Gertsch, J. C., and Bright, V. M. (**2016**). "Ultrathin thermoacoustic nanobridge loudspeakers from ALD on polyimide," Nanotechnology **27**(47), 475504.

Daschewski, M. (**2016**). "Thermophony in real gases: Theory and applications," Ph.D. thesis, Universität Potsdam, Potsdam, Germany.

De Lange, P. (**1915**). "On thermophones," Proc. R. Soc. London A **91**(628), 239–241.

Galbraith, J., Dunn, O. J., and Clark, V. A. (**1975**). "Applied statistics: Analysis of variance and regression," J. R. Stat. Soc. **138**(2), 259.

Guiraud, P., Giordano, S., Bou Matar, O., Pernod, P., and Lardat, R. (**2019a**). "Multilayer modeling of thermoacoustic sound generation for thermophone analysis and design," J. Sound Vib. **455**, 275–298.

Guiraud, P., Giordano, S., Bou Matar, O., Pernod, P., and Lardat, R. (**2019b**). "Two temperature model for thermoacoustic sound generation in thick porous thermophones," J. Appl. Phys. **126**(16), 165111.

Gustafson, J. L. (**1988**). "Reevaluating Amdahl's law," Commun. ACM **31**(5), 532–533.

Hu, H., Wang, D., and Wang, Z. (**2014**). "Solution for acoustic field of thermo-acoustic emission from arbitrary source," AIP Adv. **4**(10), 107114.

Hu, H., Wang, Y., and Wang, Z. (**2012a**). "Wideband flat frequency response of thermo-acoustic emission," J. Phys. D: Appl. Phys. **45**(34), 345401.

Hu, H., Wang, Z., Wu, H., and Wang, Y. (**2012b**). "Analysis of spherical thermo-acoustic radiation in gas," AIP Adv. **2**(3), 032106.

Hu, H., Zhu, T., and Xu, J. (**2010**). "Model for thermoacoustic emission from solids," Appl. Phys. Lett. **96**(21), 214101.

Julius, S., Gold, R., Kleiman, A., Leizeronok, B., and Cukurel, B. (**2018**). "Modeling and experimental demonstration of heat flux driven noise cancellation on source boundary," J. Sound Vib. **434**, 442–455.

Landau, L. D., and Lifschitz, E. M. (**1986a**). *Fluid Mechanics, Course of Theoretical Physics*, 3rd ed. (Butterworths Heinemann, London), Vol. 6.

Landau, L. D., and Lifschitz, E. M. (**1986b**). *Theory of Elasticity, Course of Theoretical Physics*, 3rd ed. (Butterworths Heinemann, London), Vol. 7.

Lasance, C. (**2004**). "The thermal conductivity of silicon dioxide," https://www.electronics-cooling.com/2004/08/the-thermal-conductivity-of-silicon-dioxide/ (Last viewed February 14, 2023).

Lim, C. W., Tong, L. H., and Li, Y. C. (**2013**). "Theory of suspended carbon nanotube thinfilm as a thermal-acoustic source," J. Sound Vib. **332**(21), 5451–5461.

Liu, Y. S., Tong, L. H., and Lai, S. K. (**2018**). "Thermo-acoustics generated by periodically heated thin line array," J. Sound Vib. **427**, 28–40.

MacDonald, S. (**2020**). "Sound fields: Free versus diffuse field, near versus far field," https://community.sw.siemens.com/s/article/sound-fields-free-versus-diffuse-field-near-versus-far-field (Last viewed December 1, 2021).

McDonald, F. A., and Wetsel, G. C. J. (**1978**). "Generalized theory of the photoacoustic effect," J. Appl. Phys. **49**(4), 2313–2322.

Niskanen, A. O., Hassel, J., Tikander, M., Maijala, P., Grönberg, L., and Helistö, P. (**2009**). "Suspended metal wire array as a thermoacoustic sound source," Appl. Phys. Lett. **95**(16), 163102.

Salençon, J. (**2001**). "Handbook of continuum mechanics," in *Handbook of Continuum Mechanics* (Springer-Verlag, Berlin Heidelberg).

Shinoda, H., Nakajima, T., Ueno, K., and Koshida, N. (**1999**). "Thermally induced ultrasonic emission from porous silicon," Nature **400**(6747), 853–855.

Sterling, T., Anderson, M., and Brodowicz, M. (**2018**). "High performance computing," in *High Performance Computing* (Elsevier, Amsterdam).

Taylor, B. N., and Kuyatt, C. E. (**1994**). "Guidelines for evaluating and expressing the uncertainty of NIST measurement results," NIST Technical Note 1297 (National Institute of Standards and Technology, Gaithersburg, MD).

Teichert, C., MacKay, J. F., Savage, D. E., Lagally, M. G., Brohl, M., and Wagner, P. (**1995**). "Comparison of surface roughness of polished silicon wafers measured by light scattering topography, soft-x-ray scattering, and atomic-force microscopy," Appl. Phys. Lett. **66**(18), 2346–2348.

Tong, L. H., Lim, C. W., Lai, S. K., and Li, Y. C. (**2015**). "Gap separation effect on thermoacoustic wave generation by heated suspended CNT nano-thinfilm," Appl. Therm. Eng. **86**, 135–142.

Vesterinen, V., Niskanen, A. O., Hassel, J., and Helistö, P. (**2010**). "Fundamental efficiency of nanothermophones: Modeling and experiments," Nano Lett. **10**(12), 5020–5024.

Wente, E. C. (**1922**). "The thermophone," Phys. Rev. **19**(4), 333–345.

Xiao, L., Chen, Z., Feng, C., Liu, L., Bai, Z.-Q., Wang, Y., Qian, L., Zhang, Y., Li, Q., Jiang, K., and Fan, S. (**2008**). "Flexible, stretchable, transparent carbon nanotube thin film loudspeakers," Nano Lett. **8**(12), 4539–4545.

Xiao, L., Liu, P., Liu, L., Li, Q., Feng, Z., Fan, S., and Jiang, K. (**2011**). "High frequency response of carbon nanotube thin film speaker in gases," J. Appl. Phys. **110**(8), 084311.

Yin, Y., and Hu, H. (**2017**). "Analysis of cylindrical thermo-acoustic radiation in gas," AIP Conf. Proc. **1829**(1), 020033.